Carbonyl Carbon Probe of Local Mobility in $^{13}C,^{15}N$-Enriched Proteins Using High-Resolution Nuclear Magnetic Resonance

Kwaku T. Dayie[†] and Gerhard Wagner*

Contribution from the Committee on Higher Degrees in Biophysics, Harvard University and Department of Biological Chemistry and Molecular Pharmacology, Harvard Medical School, 240 Longwood Avenue, Boston, Massachusetts 02115

Received September 27, 1996. Revised Manuscript Received May 23, 1997[⊗]

Abstract: The utility of carbonyl carbons as probes of internal mobility in proteins is investigated by theoretical and experimental methods. In a double $^{13}C,^{15}N$-labeled sample, the relaxation of the carbonyl carbon is mediated by dipolar interactions with nearby protons, the $^{13}C^{\alpha}$ and ^{15}N nuclei, and the ^{13}C chemical shielding anisotropy (CSA). Expressions are presented for carbonyl single-spin, carbonyl-nitrogen, and carbonyl-α-carbon two-spin rates due to dipolar interaction and a CSA tensor. We show that, at high magnetic fields, useful relations between relaxation rates and spectral density functions can be derived, because the CSA autocorrelation dominates carbonyl relaxation. Proton-detected $^{13}C,^{15}N$ NMR spectroscopy is used to measure one-spin carbonyl and two-spin carbonyl-nitrogen relaxation rates. Measurements are performed at 9.4, 11.7, and 17.6 T for carbonyl carbons in villin 14T, the N-terminal 14 kDa domain of the actin-binding protein villin. Three rate measurements are used to obtain the values of the spectral density function at zero [$J(0)$], nitrogen [$J(\omega_N)$], and carbonyl [$J(\omega_C)$] frequencies. The different secondary structural elements such as α-helices, β-sheets, and regions of low persistent structure have distinctive dynamic behavior that the values of the spectral density function at low frequencies (<75 MHz) reveal. The value of $J(0)$ is especially sensitive to both rapid and slow internal motions and is discussed in detail. Comparison with ^{15}N-only data indicates that one can obtain similar dynamic information from the carbonyl data. In addition, carbonyl NMR studies are potentially useful for probing hydrogen-bond dynamics, as significantly different average $J(0)$ values were observed for hydrogen-bonded and solvent-exposed carbonyls.

I. Introduction

Nuclear spin relaxation measurements are ideal to probe the vast time range of molecular motions from picosecond to millisecond.[1,2] To date, relaxation studies of internal motions in proteins have primarily focused on ^{15}N nuclei; recently, however, attention has began shifting to ^{13}C nuclei.[3] Here, we choose to focus on the carbonyl carbon as a direct probe of structural mobility. This has advantages from both spectroscopic and structural perspectives. A narrow spectral dispersion (10 ppm) and the relative spectral isolation from any *J*-coupled neighbors (120 ppm far removed from aliphatic region) facilitates application of selective pulses and decoupling from other carbon nuclei. The large chemical shielding anisotropy (CSA) coupling constant of the carbonyl carbons (>140 ppm) makes the CSA mechanism dominant at high magnetic fields and thus the interpretation of the data tractable. Structurally, carbonyl groups are the most important hydrogen-bond acceptors in proteins; they form such bonds in regular secondary structural elements such as α-helices and β-sheets.

In this paper, we present a comprehensive analysis of carbonyl carbon as a useful probe of dynamics in proteins. In section II, four experiments are proposed to measure the relaxation rates of transverse inphase coherence $^{13}C'_x$,[4] longitudinal one-spin order C'_z,[4] the decay rates of transverse antiphase coherence $2N_zC'_x$, and longitudinal two-spin order $2N_zC'_z$. The theoretical framework for analyzing carbonyl relaxation experiments is briefly summarized in section III using established methods.[5] Analytic expressions describing the carbonyl carbon relaxation dynamics involving both self and cross-correlation effects are summarized in Table 1. This part includes a simulation using the method of perturbing the matrix exponential[6] to gauge the relative importance of possible cross-relaxation pathways. Such considerations are used in the design of four pulse sequences for measuring the carbonyl decay rates. This section also contains a simple scheme for characterizing the internal motions in biomolecules from any three of the four sets of rate measurements. Results of the proposed scheme are shown for the actin-severing protein villin 14T with the experiments performed at three spectrometer frequencies of 9.4, 11.7, and 17.6 T. These results are compared with previous ^{15}N-only study,[7] and the similarities and differences between the two approaches are outlined.

II. Experimental Aspects

Uniformly $^{15}N,^{13}C$-enriched villin 14T, the N-terminal 126-residue domain of the actin-binding protein villin 14T, was produced and purified as described previously.[7] A 2.5 mM sample at pH 4.4 and

* Author to whom correspondence should be addressed.

[†] Present Address: Chemistry Department, Massachusetts Institute of Technology, 77 Massachussetts Avenue, Bldg 56-546, Cambridge, Massachusetts 02139.

[⊗] Abstract published in *Advance ACS Abstracts,* August 1, 1997.

(1) Brooks, C. L., III; Karplus, M.; Pettitt, B. M. *Proteins: A Theoerectical Perspective of Dynamics, Structure, and Thermodynamics*; John Wiley and Sons: New York, 1988; pp 1−259.

(2) Tycho, R., Ed.; *Understanding Chemical Reactivity: Nuclear Magnetic Resonance Probes of Molecular Dynamics*; Kluwer Academic Publishers: Boston, 1994; pp 1−550.

(3) (a) Palmer, A. G. III *Curr. Opin. Biotechnol.* **1993**, *4*, 385−391. (b) Dayie, K. T.; Wagner, G.; Lefèvre, J.-F. *Ann. Rev. Phys. Chem.* **1996**, *47*, 243−282.

(4) Dayie, K. T.; Wagner, G. *J. Magn. Reson. B*, **1995**, *109*, 105−108.

(5) (a) Abragam, A. *The Principles of Nuclear Magnetism*; Clarendon Press: Oxford, 1961; Chapter VIII. (b) Haeberlen, U. *High Resolution NMR in Solids: Selective Averaging;* Academic Press: New York, 1976; Chapter II. (c) Spiess, H. W. *NMR Basic Princ. Prog.* **1978**, *15*, 55−214. (d) Goldman, M. *J. Magn. Reson.* **1984**, *60*, 437−452.

(6) Najfeld, I.; Havel T. F. *Adv. Appl. Math.* **1995**, *16*, 321−375.

(7) (a) Markus, M. A.; Dayie, K. T.; Matsudaira, P.; Wagner, G. *Biochemistry* **1996**, *35*, 1722−1732. (b) Markus, M. A.; Nakayama, T.; Matsudaira, P.; Wagner, G. *Protein Sci.* **1994**, *3*, 70−81.

S0002-7863(96)03388-4 CCC: $14.00

Table 1. Rate Expressions for the Various Spin Orders Involving the Carbonyl Carbons for Dipolar and Chemical Shift Anisotropy Relaxation Processes

(i) Dipolar Relaxation[a]

$$R_{c'}(C'_z) = \sum_j D_{c'j}\,[J(\omega_j - \omega_{c'}) + 3J(\omega_{c'}) + 6J(\omega_j + \omega_{c'})]$$

$$R_{c'}(C'_x) = {}^1/_2 \sum_j D_{c'j}\,[4J(0) + J(\omega_j - \omega_{c'}) + 3J(\omega_{c'}) + 6J(\omega_j + \omega_{c'}) + 6J(\omega_j)]$$

$$R_{c'P}(2P_zC'_z) = D_{c'P}\,[3J(\omega_{c'}) + 3J(\omega_P)] + \sum_i D_{Pi}\,[3J(\omega_i) + 3J(\omega_P)]$$

$$R_{c'P}(2P_zC'_x) = {}^1/_2 \sum_j D_{c'j}\,[4J(0) + J(\omega_j - \omega_{c'}) + 3J(\omega_{c'}) + 6J(\omega_j + \omega_{c'})] + \sum_i D_{Pi}\,[3J(\omega_i) + 3J(\omega_P)]$$

$$R_{c'}(j \rightarrow C'_z) = D_{c'j}\,[6J(\omega_j + \omega_{c'}) - J(\omega_j - \omega_{c'})]$$

(ii) Chemical Shift Anisotropy for Isotropic Spherical Top Tumbler[b]

$$R_{C'}(C'_z) = \frac{\omega_{C'}{}^2\Delta\sigma_g{}^2}{3} J(\omega_{C'})$$

$$R_{C'}(C'_x) = \frac{\omega_{C'}{}^2\Delta\sigma_g{}^2}{3}\,[{}^2/_3 J(0) + {}^1/_2 J(\omega_{C'})]$$

$$R_{C'}(2N_zC'_x) = \frac{\omega_{C'}{}^2\Delta\sigma_g{}^2}{3}\,[{}^2/_3 J(0) + {}^1/_2 J(\omega_{C'})] + \frac{\omega_N{}^2\Delta\sigma_N{}^2}{3} J(\omega_N)$$

$$R_{C'N}(2N_xC'_z) = \frac{\omega_N{}^2\Delta\sigma_N{}^2}{3}\,[{}^2/_3 J(0) + {}^1/_2 J(\omega_N)] + \frac{\omega_{C'}{}^2\Delta\sigma_g{}^2}{3} J(\omega_{C'})$$

$$R_{C'C^\alpha}(2C^\alpha{}_zC'_z) = \frac{\omega_{C'}{}^2\Delta\sigma_g{}^2}{3} J(\omega_{C'}) + \frac{\omega_{C^\alpha}{}^2\Delta\sigma_c{}^2}{3} J(\omega_C)$$

$$R_{C'C^\alpha}(2C^\alpha{}_xC'_z) = \frac{\omega_{C^\alpha}{}^2\Delta\sigma_c{}^2}{3}\,[{}^2/_3 J(0) + {}^1/_2 J(\omega_C)] + \frac{\omega_{C'}{}^2\Delta\sigma_g{}^2}{3} J(\omega_{C'})$$

$$R_{C'N}(2N_zC'_z) = \frac{\omega_{C'}{}^2\Delta\sigma_g{}^2}{3} J(\omega_{C'}) + \frac{\omega_N{}^2\Delta\sigma_N{}^2}{3} J(\omega_N)$$

(iii) Dipolar − CSA Interference[c]

$$R_{c'j}(C'_z \leftrightarrow 2j_zC'_z) = K_1{}^{c'j}\,J^1(\omega_{c'}) + K_2{}^{c'j}J^2\,(\omega_{c'})$$

$$R_{c'j}\,(C'_x \leftrightarrow 2j_z{}^\alpha\,C'_x) = {}^2/_3 J(0)\{K_1{}^{c'j} + K_2{}^{c'j}\} + {}^1/_2\{K_1{}^{c'j}J^1(\omega_{c'}) + K_2{}^{c'j}J^2(\omega_{c'})\}$$

[a] $j = \{^{15}N, ^{13}C^\alpha, H^N, H^\alpha, H^{hb}\}$, i indexes all nuclei dipolar-coupled to the P atom (^{13}C or ^{15}N), such as H^N, H^α, and H^{hb}; D_{ij} are the dipolar coupling constants between the two nuclei i and j, $D_{ij} = (\hbar^2\gamma_i{}^2\gamma_j{}^2)/4r_{ij}{}^6$). [b] $\Delta\sigma_c{}^2$, $\Delta\sigma_g{}^2$, and $\Delta\sigma_N{}^2$ are, respectively, the CSA constants for $^{13}C^\alpha$, $^{13}C'$, and ^{15}N nuclei. The generalized CSA constant $\Delta\sigma_g{}^2$ is defined in eq 1. More general expressions for anisotropic motion can be found in the literature (see e.g. ref 15). [c] The coupling constants are defined as: $K_1{}^{c'j} = (\hbar\gamma_{c'}\gamma_j\Delta_1\omega_{c'}\langle P_2\,(\cos(\Phi_1))\rangle)/r_{c'j}{}^3$; $K_2{}^{c'j}) = (\hbar\gamma c'\gamma_j\Delta_2\omega_{c'}\langle P_2(\cos(\Phi_2))\rangle)/r_{c'j}{}^3]$, Φ_i is the angle between the C′−j internuclear vector and the principal direction of the shielding tensor. $\langle P_2(\cos(\Phi_i)\rangle$ is the ensemble average of the second order Legendre polynomial as a function of this angle Φ_i. A similar tabulation can be found in ref 15c.

298 K was used. The sample was degassed and sealed under argon prior to the measurements.

Four pulse sequences (Figure 1) were designed to measure the rate of decay of C'_z, C'_x, and the two spin order terms $2C'_zN_z$ and $2C'_xN_z$ based on straightforward modifications of the HNCO experiment.[8] Details of the design strategy are given in section III. All four pulse sequences include water flip back pulses. For the measurements of transverse relaxation rates (Figure 1C,E), continuous wave spin locks are applied during the relaxation delays T.

All the experiments were carried out on Varian Unity plus 400, Unity 500, and UNITY plus 750 MHz spectrometers equipped with pulsed field gradient units and triple-resonance probes with actively shielded z-gradients. Each time point typically took 2 h to complete except for the long mixing times used for the measurements of longitudinal relaxation rates, $R_{c'}(C'_z)$, which took up to 4 h. Alternatively, the experiments could be started directly on the carbonyl carbons. This was especially necessary at higher magnetic fields (>14.1 T). Starting directly on the carbons shortens the sequence and therefore leads to increased signal-to-noise, and losses to relaxation are minimized. The experimental time, however, increases since longer recycle delays are needed due to the very slow longitudinal relaxation of carbonyls.

Each data set consisted of 100−122 complex time points in the indirect dimension and 2K points in the direct dimension. For the spin lock experiments 3−3.5 kHz fields were typically employed. For longitudinal $^{13}C'$ relaxation rate $R_{c'}(C'_z)$, the delays used at 400 MHz were 10, 60(2x), 120, 240, 480, 2000, 4000, and 5000 ms; at 500 MHz the delays were 64(2x), 128, 256, 400, 1000, and 1500 ms; and at 750 MHz the delays were 10.1(2x), 40.3, 60.5, 80.7, 161.4, 322.8, 907.7, 2582.0, and 4034.4 ms. For longitudinal two-spin order rate $R_{c'N}(2N_zC'_z)$, the delays used at 400 MHz were 10, 40(2x), 80, 120, 200, 400, and 600 ms; at 500 MHz these were 10(2x), 50, 100, 250, 600, and 1000 ms; and at 750 MHz they were 40(2x), 80, 160, 240, 400, and 600 ms. For transverse in-phase rate $R_{c'}(C'_x)$, the delays used at 400 MHz were 4.19, 8.38(2x), 16.77, 33.54, 67.07, and 134.14 ms; at 500 MHz these were 6, 10, 20(2x), 30, 40, 60, 80, and 100 ms; and at 750 MHz they were 8.64(2x), 11.52, 17.28, 23.04, 46.08, and 69.12 ms. Finally, for the transverse antiphase rate $R_{c'N}(2N_zC'_x)$, the delays used were at 500 MHz 5.96, 14.81(2x), 29.53, 47.19, 73.68, and 117.85 ms and at 750 MHz 5.76, 11.52(2x), 23.04, 34.56, 46.08, and 92.16 ms. Each

(8) (a) Muhandiram, D. R.; Kay, L. E. *J. Magn. Reson. B.* **1994**, *103*, 203−216. (b) Kay, L. E.; Ikura, M.; Tschudin, R.; Bax, A. *J. Magn. Reson.* **1990**, *89*, 496−514.

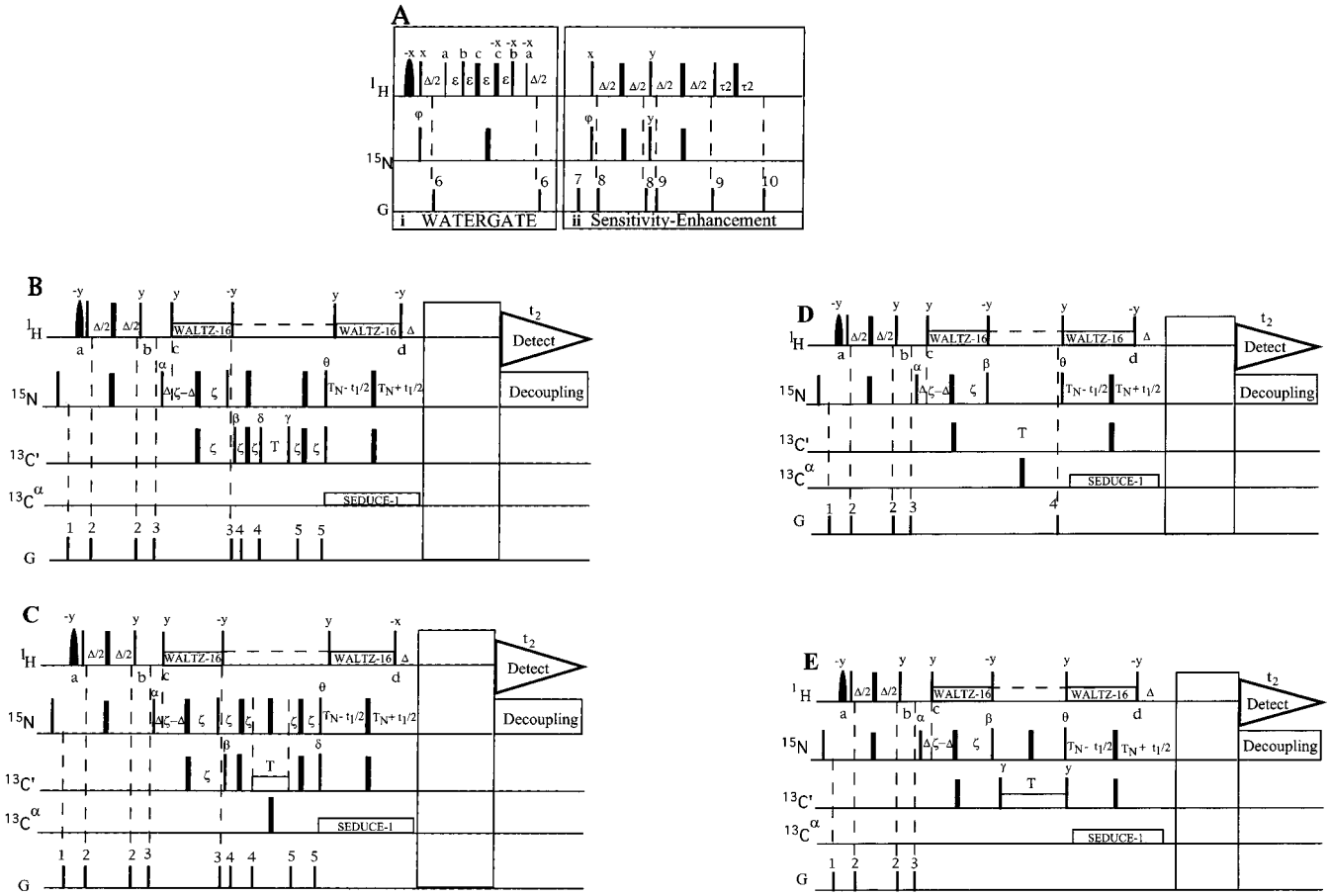

Figure 1. Two-dimensional heteronuclear pulse sequences for measuring four carbonyl relaxation rates along the protein backbone. Darkened thin and thick vertical bars represent 90° and 180° pulses, respectively. WALTZ-16[24] decoupling at 6kHz is applied on the ^{1}H channel to maintain the transverse nitrogen magnetization inphase; during acquisition a 1.5 kHz field is applied to the nitrogen channel. Selective pulses applied at the water resonance use a full-Gaussian or rectangular pulse of ~2 ms duration. All selective pulses are 90° rotations. During the constant time ^{15}N evolution period a SEDUCE-1[25] decoupling train is applied to the $^{13}C^{\alpha}$ spins using a 90° pulse of 331ms or an MLEV square modulation (+ + - -) superimposed on the i-SNOB-3 decoupling waveform generated using the Pbox utility.[26] The delay Δ is set to slightly less than $^1/_2J_{HN}$ at 5.6 ms, τ_2 to 0.13 ms, and ζ and T_N to 12.4 ms. (**A**) Any of the two modules can be substituted in the rectangular open boxes shown in subsequent pulse sequences in **B**−**E**. **i.** WATERGATE.[27] $\epsilon = [\Delta/2 - 1.69\nu)]$ where ν is the inverse of the frequency offset from the water resonance at which the 3−9−19 selective sequence delivers maximum excitation (ν = 210−300 μs); a, b, and c correspond to the 3/13, 9/13, and 19/13 X π/2 proton pulses. The duration and strength of G_6 is 1 ms and 0.156 T m^{-1}. **ii**. Preservation of Coherence pathway.[28] Two fids are acquired for each increment of t_1 with the amplitude of G_7 and the phases φ inverted in the second fid. The gradients G_7 and G_{10} are used for coherence selection: their durations and strengths are G_7 1.3 ms, 0.3 T m^{-1}; G_{10} 0.13 ms, 0.289 T m^{-1}. G_8 and G_9 are clean-up gradients of 0.5 ms at 0.05−0.1 T m^{-1}. (**B**) $R_{C'}(C'_z)$, the decay rate of the longitudinal one-spin order (modified from ref 4). (**C**) $R_{C'}(C'_x)$ the decay rate of the transverse magnetization. (adapted from ref 4). (**D**) $R_{C'N}(2C'_zN_z)$, the decay rate of the longitudinal two-spin order or the *J*-ordered state. (**E**) $R_{C'N}(2C'_xN_z)$ the decay rate of the antiphase two-spin order. All nonlabeled pulses are applied along the x-axis. All other gradients are applied for about 500 μs at 0.05−0.08 T m^{-1}. The delay during which the spin order decays is labeled *T* in all of the pulse sequences. Note that we spin lock the relaxing coherences in **C** and **E**, indicated with open boxes, using continuous wave pulses. The phase cycle used is as follows: $\alpha = x, -x$; $\beta = [2x, 2(-x)]$. (**A**) i. $\varphi = x$. ii. $\varphi = x$ for first fid and $\varphi = -x$ for second fid. (**B**) $\delta = 4y, 4(-y)$; $\gamma = y$; $\theta = [8x, 8(-x)]$; rec = $[(x, -x, -x, x), 2(-x, x, x, -x), (x, -x, -x, x)]$. (**C**) $\delta = [4x, 4(-x)]$; $\theta = [8x, 8(-x)]$; rec = $[(x, -x, -x, x), 2(-x, x, x, -x), (x, -x, -x, x)]$; (**D**) $\theta = [4x, 4(-x)]$; rec = $(x, -x, -x, x), (-x, x, x, -x)$. (**E**) $\gamma = 4y, 4(-y)$; $\theta = [8x, 8(-x)]$; rec = $[(x, -x, -x, x), 2(-x, x, x, -x), (x, -x, -x, x)]$. During the measurements, the WALTZ decoupling of the protons can be left on; it does not influence the rates. During the decoupling, gradient pulses are not applied. The long blank rectangular boxes represent either of the two modules for water suppression shown in **A**.

spectrum was processed using Felix 2.1 on Silicon Graphics IRIS 4D-35 workstations: each fid was zero-filled to 8 K, a 45°-shifted sine-squared function was applied prior to strip transformation; interferograms in t_1 were zero-filled to 512 real points and a 45−60°-shifted sine-squared function applied before Fourier transformation. Examples of relaxation curves depicting the decay of $2N_zC'_z$ and $2N_zC'_x$ magnetization with time for Asn 85 are shown in Figure 2. Relaxation rates were determined as described previously:[9] the Levenburg−Marquardt algorithm[10] was used to fit the exponential decays in a nonlinear least-squares fashion; Monte Carlo procedures, based on the difference between repeated data points as the standard deviation of the presumed Gaussian distribution, were used to estimate the errors; these estimated errors were taken to be the standard deviations from an ensemble of 500 synthetically generated data sets. Spectral density values were calculated by inverting eq 8 using routines in MATLAB[11] and the error estimates (δJ) were computed by a simple propagation of errors in the rate measurement uncertainties[12]

III. Theorectical Aspects: Mechanisms Relevant for Carbonyl Relaxation

Expressions of relaxation rates for different nuclei have appeared extensively in the literature (see e.g. ref 2). We

(9) Peng, J. W.; Wagner, G. *J. Magn. Reson.* **1992**, *98*, 308−332.

(10) Press, W. H.; Flannery, B. P.; Teukolsky, S. A. *Numerical Recipes in C- The Art of Scientific Computing*; Cambridge University Press: New York, 1988; pp 1−735.

(11) MATLAB, Mathworks, Natick, MA 1995.

(12) Bevington, P. R. *Data Reduction and Error Analysis for the Physical Sciences*; McGraw-Hill Book Company: New York, 1969; Chapter 4.

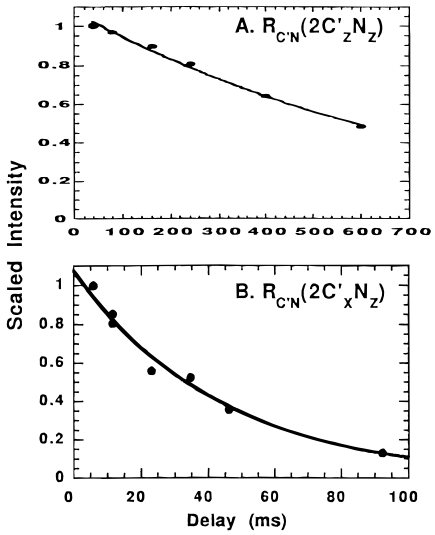

Figure 2. Typical decay curves for Asn85 using the pulse sequences shown in Figure 1 D,E. Peak intensities were measured by integrating cross-peaks along the $^1H(F_2)$ dimension through the peak maxima. (**A**) $R_{C'N}(2C'_zN_z)$ fit consisting of seven data points at 40(2*x*), 80, 160, 240, 400, and 600 ms. (**B**) $R_{C'N}(2C'_xN_z)$ fit consisting of eight data points at 5.76, 11.52(2*x*), 23.04, 34.56, 46.08, and 92.16 ms.

specialize some of these results for the auto-, cross-, and cross-correlation relaxation rates of the carbonyl carbons using established methods.[5] For a doubly labeled $^{15}N-^{13}C$ protein molecule, four classes of contributors to the carbonyl relaxation dynamics include: dipolar autocorrelation, CSA autocorrelation, dipolar−CSA interference, and dipolar−dipolar interference.

(i) Dipolar Autocorrelation. For dipolar autocorrelation, the following nuclei significantly participate in the dipolar interaction with the carbonyl carbons: ^{15}N, $^{13}C^{\alpha}$, H^N, H^{α}, H^{hb}; H^N, H^{α}, and H^{hb} are respectively the amide, α, and hydrogen-bonded protons. The resulting rate expressions for various spin orders [e.g. $Q = {}^{13}C'_z$, $^{13}C'_x$, $2C'_zP_z$, $2C'_xP_z$] that account for these different contributions are given in Table 1 (P is ^{13}C or ^{15}N).

(ii) CSA Autocorrelation. For the CSA autocorrelation, the CSA tensor of the carbonyl carbon is nonsymmetric. Following the strategy of Goldman,[5d] the lattice variables are separated from the spin variables, and the asymmetric chemical shielding tensor decomposed into an isotropic and two axially symmetric anisotropic terms with the symmetry axes arbitrarily chosen as the two principal axes along *X* and *Y*.[5b,d] The choice of the two symmetry axes is entirely arbitrary, and therefore for this work, we define a generalized CSA coupling constant, $\Delta\sigma_g$, that makes use of the equivalence of the following representations:

$$\begin{aligned}\Delta\sigma_g^2 &= \Delta_1^2 + \Delta_2^2 - \Delta_2\Delta_1 \\ &= [(\sigma_{xx}-\sigma_{zz})^2 + (\sigma_{yy}-\sigma_{zz})^2 + (\sigma_{yy}-\sigma_{xx})^2]/2 \\ &= \sigma_{xx}^2 + \sigma_{yy}^2 + \sigma_{zz}^2 - \sigma_{yy}\sigma_{xx} - \sigma_{yy}\sigma_{zz} - \sigma_{xx}\sigma_{zz} \\ &= 3[(\sigma_{xx}-\sigma_{iso})^2 + (\sigma_{yy}-\sigma_{iso})^2 + (\sigma_{yy}-\sigma_{iso})^2]/2 \\ &= \Delta\sigma_{CR}^2(1+\eta^2/3) \qquad (1)\end{aligned}$$

The expressions on the right-hand side of eq 1 correspond to the different definitions used in the literature, $\Delta_1 = \sigma_{xx} - \sigma_{zz}$ and $\Delta_2 = \sigma_{yy} - \sigma_{zz}$;[5d] σ_{iso} is the arithmetic mean of the diagonal elements of the symmetric portion of the CSA tensor in its principal axis system;[13] and $\Delta\sigma_{CR} = \sigma_{zz} - (\sigma_{yy} + \sigma_{xx})/2$ and $\eta = 3(\sigma_{xx} - \sigma_{yy})/2\Delta\sigma_{CR}$.[14] Goldman's strategy allows us to derive the rate expressions for the general case and simplified expressions that arise for an isotropic spherical tumbler. The expressions for anisotropic motion beome unwieldy, and these can be found in the literature.[15]

Following Goldman's approach, one sees that the effective spectral density function consists of three terms:

$$J^{effCSA}(\omega) = a_1^{c'}J^{CSA(1)}(\omega) + a_2^{c'}J^{CSA(2)}(\omega) + a_3^{c'}J^{CSA(1)-CSA(2)}(\omega) \quad (2)$$

The CSA coupling constants are defined as $a_1^{c'} = \omega_2^{c'}\Delta_1^2/3$, $a_2^{c'} = \omega_2^{c'}\Delta_2^2/3$, $a_3^{c'} = -\omega_2^{c'}\Delta_1\Delta_2/3$. ω_c' is the $^{13}C'$ Larmor frequency. With these definitions and the implicit assumption of spherical top molecular diffusion, we obtain the simpler rate expression for the different spin orders (Q):

$$R_Q(Q_n) = \frac{5}{h^2}\sum_{q=-1}^{1}\begin{pmatrix}1 & 1 & 2\\ 0 & q & -q\end{pmatrix}\cdot{}^2\mathrm{Tr}\{[(K_q^2)^{\dagger},[K_q^2,Q_n]]\}\sum_i a_i J^i(q\omega_{C'}) \quad (3)$$

Tr stands for the trace operation. [*K*] is associated with the spin angular momentum operators. For the approximately axially symmetric tensor of the ^{15}N nuclei, $a^N = \omega_N^2\Delta_N^2/3$; $\Delta_N = \sigma_{||} - \sigma_{\perp}$, and ω_N is the ^{15}N Larmor frequency. The summation over i runs over the three terms of eq 2. The results for the various spin orders are summarized in Table 1.

(iii) Dipolar−CSA Interference. Because both CSA and dipolar mechanisms depend on second rank tensors with similar rotational properties, interferences can arise between the two mechanisms involving the shared carbonyl carbon atom. The following interconversions may become active under such an interference: $C'_z \leftrightarrow 2N_zC'_z$, $C'_x \leftrightarrow 2N_zC'_x$, $C'_z \leftrightarrow 2C_z^{\alpha}C'_z$, and $C'_x \leftrightarrow 2C_z^{\alpha}C'_x$. Expressions for the Dipolar-CSA interference terms are listed in Table 1.

(iv) Dipolar Interference. Possible cross-relaxation processes can occur when two heteronuclear dipolar interactions such as $^{13}C'-^{15}N$ and $^{13}C'-^{13}C^{\alpha}$ are modulated in a correlated manner such that the interconversion $C'_z \leftrightarrow 4M_zP_zC'_z$, for example, is allowed. M and P belong to any one in the set $\{^{13}C^{\alpha}, H^{\alpha}, H^N$, and $^{15}N\}$. This general phenomenon involves any set of correlated dipolar vectors such as $^{13}C'-^{15}N \leftrightarrow {}^{13}C'-H^N$, $^{13}C'-^{15}N \leftrightarrow {}^{13}C'-H^{\alpha}$, $^{13}C'-^{13}C^{\alpha} \leftrightarrow {}^{13}C'-H^{\alpha}$, $^{13}C'-H^N \leftrightarrow {}^{13}C'-H^{\alpha}$, $^{13}C'-^{15}N \leftrightarrow {}^{13}C'-^{13}C^{\alpha}$. Pulse sequences can be designed to measure these rates, or one can suppress these pathways to simplify the time dependence of the relaxation events. In the following section, the magnitudes of these cross-relaxation processes are considered in some detail.

(v) Relative Strength of Each Contributing Mechanism. Applications of expressions in Table 1 help to establish the significance of each contributing pathway for the different relaxation mechanisms. Figure 3 shows the relative strength of each relaxation mechanism represented by the magnitude of each relaxation coupling constant: dipolar-only (*D*), CSA-only,

(13) Norton, R. S.; Clouse, A. O.; Addleman, R.; Allerhand, A. *J. Am. Chem. Soc.* **1977**, *99*, 79−83.

(14) Canet, D.; Robert, J. B. In *NMR, Basic Principles and Progress;* Diehl, P., Fluck, E.,Günther, H., Kosfeld, R., Seelig, J., Eds.; Springer: Berlin, 1991; pp 45−89.

(15) (a) Chung, J.; Oldfield, E.; Thevand, A.; Werbelow, L. G. *J. Magn. Reson.* **1992**, *100*, 69−81. (b) Werbelow, L. G. In *Understanding Chemical Reactivity: Nuclear Magnetic Resonance Probes of Molecular Dynamics*; Tycho, R., Ed.; Kluwer Academic Publishers: Boston, 1994; pp 223−263. (c) Werbelow, L. G. In *Encyclopedia of NMR*; Harris, R. K., Grant, D. M., Eds.; John Wiley and Sons: Chichester, U.K., 1996; pp 4072−4078.

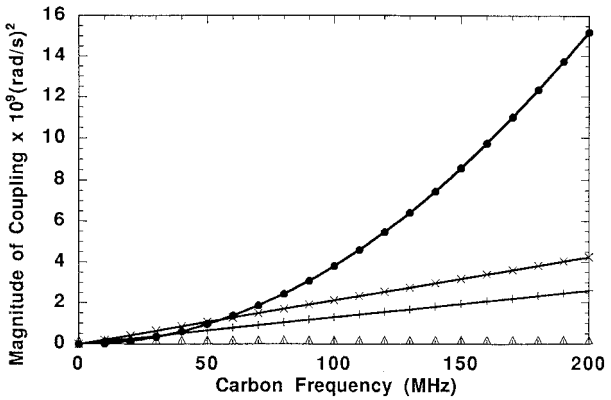

Figure 3. Simulation of the relative strengths of each relaxation mechanism [$\times 10^9$ (rad/s)^2] vs carbon spectrometer frequency (MHz). (●) Carbonyl CSA only (C_1 in Table 2). (×) Estimate of the maximum contribution of the CSA-DD cross-correlation between $^{13}C'$ and $^{13}C^{\alpha}$ (K_1 in Table 1 assuming $\Phi_1 = 0°$), (+) Estimate of the maximum contribution of the CSA-DD cross-correlation between $^{13}C'$ and ^{15}N (K_1 in Table 1 assuming $\Phi_1 = 0°$), and (△) sum of dipolar contributions (D_1 in Table 2). The following internuclear distances and chemical shielding values were used:[29] $r_{C'N} = 1.32$ Å, $r_{C'-C^{\alpha}} = 1.51$ Å, $r_{C'-H^N} = 2.64$ Å, $r_{C'-H^{\alpha}} = 2.12$Å, $r_{C'-H^{hbond}} = 3.0-3.6$ Å, $\gamma_H = 26.7519 \times 10^7$ rad (Ts)$^{-1}$, $\gamma_C = 6.7283 \times 10^7$ rad (Ts)$^{-1}$; and $\gamma_N = -2.712 \times 10^7$ rad (Ts)$^{-1}$. A generalized CSA constant of 170 ppm is used for the carbonyl carbons and 160 ppm for the ^{15}N nuclei.

cross-terms due to CSA−dipolar (CSA-D), and dipolar−dipolar interference terms (DD). Whereas the D and DD constants are field independent and entirely negligible, the CSA and CSA-D coupling constants respectively vary quadratically and linearly with B_0. CSA-D in addition varies inversely with the cube of internuclear distances. Typical values for internuclear distances for each vector and the gyromagnetic ratios used are given in the legend to Figure 3. As can be seen from this figure, D and DD coupling terms are roughly less than 0.8−5% of those of the CSA coupling constants.

In addition, values of the spectral density function at frequencies greater than those of carbon are less than 5 and 1% those at the nitrogen and zero frequencies respectively. Considering the small contribution of the dipolar terms (<5%) and the small magnitude of the values of spectral density function for frequencies greater than those of carbon (<5%), one may discard terms involving the dipolar terms premultiplied by $J(\omega > \omega_C)$. We call this the high-frequency approximation (HFA).

(vi) Multispin Relaxation of the Carbonyl Carbons. In this section, we gauge the relative importance of possible cross-relaxation pathways using the method of the perturbing the matrix exponential,[6] a general form of perturbation analysis. We consider both longitudinal and transverse relaxation pathways, and the pulse sequences we have designed to measure the rate of decay of C'_z, C'_x, and the two spin order terms $2C'_zN_z$ and $2C'_xN_z$. The system of first-order differential equations that describe the carbonyl longitudinal magnetization is [see e.g. ref 16]:

$$\frac{d}{dt}\begin{bmatrix}\Delta C'_z \\ \Delta P_z \\ \Delta 2C'_zP_z\end{bmatrix} = -\begin{bmatrix}R_1 & \sigma & \Lambda_1 \\ \sigma & R_2 & \Lambda_2 \\ \Lambda_1 & \Lambda_2 & R_3\end{bmatrix} \times \begin{bmatrix}\Delta C'_z \\ \Delta P_z \\ \Delta 2C'_zP_z\end{bmatrix} \quad (4)$$

Here, P refers to two nuclei of interest: ^{15}N and $^{13}C^{\alpha}$. $R_i (i = 1-3)$ denotes, for example, the self-rate: $R_1 = R_{C'}(C'_z)$; $R_2 = R_P(P_z)$; $R_3 = R_{C'P}(2C'_zP_z)$. σ and $\Lambda_{1,2}$ are the cross and cross-correlation rates respectively between different spin orders, and Δ represents the deviation of the magnetization from thermal equilibrium. The detailed expressions for the rates are given in Table 1.

With the method of perturbing the matrix exponential, one obtains to second order and for short mixing times:

$$\langle C'_z(t)\rangle \approx C'^{eq}_z + \Delta C'_z(0)\exp(-R_1t) - 2C'_zP_z(0)\Lambda_1 \times [t - (R_1 + R_3)\,t^2/2\} - \Delta P_z(0)\sigma\{t - (R_1 + R_2)\,t^2/2\}$$

$$+ (^1/_2)\{\Delta C'_z(0)(\Lambda_1^2 + \sigma^2) + \Lambda_2[\Delta P_z(0)\Lambda_1 + 2C'_zP_z(0)\,\sigma]\}t^2 + \ldots \quad (5)$$

The approximation given in eq 5 provides some insight into the effects of both cross-relaxation (nuclear Overhauser effect) and the cross-correlation cross-relaxation on the cross-peak intensities. A series of 90° pulses separated by 5 ms delays saturate the $^{13}C^{\alpha}$ energy levels and minimize the contribution of some of these extraneous pathways. It is important that the $^{13}C^{\alpha}$ 90° pulse is adjusted so as to minimally perturb the carbonyl resonances. A simulation using full-matrix exponentiation, second-order, and zeroth-order approximations (Figure 4A) illustrates that for mixing times $T < 3/R_1$, reliable values can be extracted from monoexponential fits to the data.

The longitudinal two spin order couples to the Zeeman orders C'_z and P_z by CSA−dipolar cross-correlated motion (P is ^{15}N or $^{13}C^{\alpha}$). This two-spin order, at short mixing times, evolves in time as:

$$\langle 2C'_zP_z(t)\rangle \approx 2C_z'P_z(0)\exp(-R_3t)$$

$$- \Delta C'_z(0)\Lambda_1\{t - (R_1 + R_3)t^2/2\} - \Delta P_z(0)\Lambda_2\{t - (R_2 + R_3)t^2/2)\}$$

$$+ (^1/_2)\{\sigma[\Delta C'_z(0)\Lambda_2 + \Delta P'_z(0)\Lambda_1] + 2C'_zP_z(0)(\Lambda_1^2 + \Lambda_2^2)\}t^2 + \ldots \quad (6)$$

The cross-terms, therefore, may add to the cross-peak intensity. In the design of the pulse sequence, two steps can be taken to minimize this effect. First, a 90° pulse on the ^{15}N followed by a gradient before the INEPT transfer dephases the terms involving $N_z(0) - N_z^{eq}$. Second, 180° pulse on the ^{15}N during the mixing period suppresses somewhat the cross-correlation effect. Additionally, because the two spin orders involve the ^{15}N nuclei, possible cross-correlated transfers with attached amide protons can be suppressed using a decoupling sequence on the protons during the relaxation period. Simulation using full-matrix exponentiation, second-order, and zeroth-order approximations (Figure 4B) illustrate that for mixing times $T < 2/R_3$, reliable values can be extracted from monoexponential fits to the data.

Cross-correlated induced motion interconverts inphase to antiphase magnetization of the $^{13}C'$ spins such that both inphase and antiphase coherences build up (decay) biexponentially:

$$\begin{bmatrix}\langle C'_x\rangle \\ \langle 2P_zC'_x\rangle\end{bmatrix} = \exp(-(t\mathrm{Tr}\{\mathbf{V}\}/2))\,[\cosh(t\sqrt{\zeta})\cdot\mathbf{I} + \{(\sinh(t\sqrt{\zeta}))/\sqrt{\zeta}\}\cdot\mathbf{N}]S(0) \quad (7)$$

where $\mathbf{I}$ is the 2 × 2 identity matrix,

$$\mathbf{V} = \begin{bmatrix}R_x & \mu \\ \mu & R_{xz}\end{bmatrix}, \qquad \mathbf{N} = \begin{bmatrix}\delta & \mu \\ \mu & -\delta\end{bmatrix}$$

$\zeta = \delta^2 + \mu^2$, $\delta = (R_{xz} - R_x)/2$, $R_x = R_{C'}(C'_x)$, $R_{xz} = R_{C'P}(2P_zC'_x)$,

(16) (a) Elbayed, K.; Canet D. *Mol. Phys.* **1989**, *68*, 1033−1046. (b) Burghardt, I.; Konrat, R.; Bodenhausen, G. *Mol. Phys.* **1992**, *75*, 467−86.

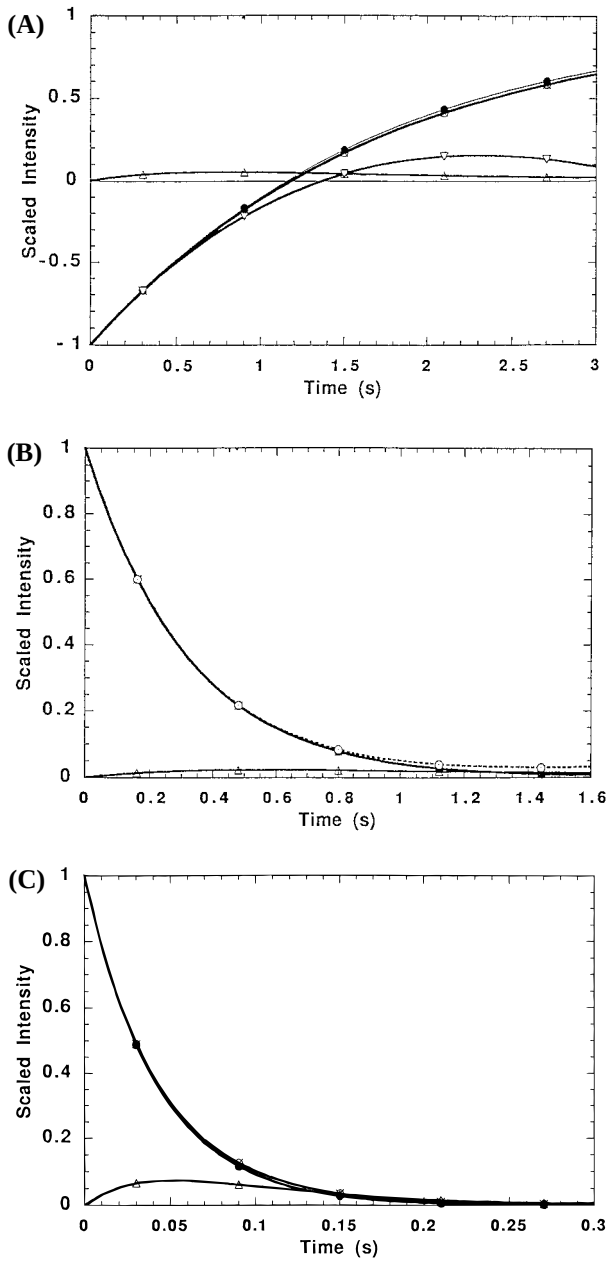

Figure 4. Simulation of the relaxation time course of spin orders involving carbonyl carbons: (**A**) Recovery of longitudinal magnetization after inversion simulated with eq 5. (●) Monoexponential approximation. (×) Full matrix exponential fit. (○) Second-order approximation. (▽) Short mixing time approximation. (Δ) Buildup of *J*-order state. (**B**) Simulation of decay of *J*-ordered state magnetization using eq 6. (•) Monoexponential approximation. (×) Full matrix exponential fit. (○) Second order approximation. (Δ) Buildup of longitudinal magnetization. (**C**) Simulation of the decay of antiphase and buildup of inphase magnetization using eq 7. (●) Monoexponential approximation. (×) Full matrix exponential fit. (○) Analytic expression. (△) Buildup of inphase magnetization.

and $\mu = R_{C'P}(C'_x \leftrightarrow 2P_zC'_x)$. Unless such effects are the aim of the study, it becomes crucial to suppress the unwanted pathway by applying 180° on the ^{15}N at the top of the spin echo.[17] However, as shown in Figure 4C, such effects are quite small, provided the cross-correlation times $T < {}^1/_4R_{x,xz}$.

(vii) Spectral Densities from Relaxation Rates. As shown previously,[18] a set of six rates enables the calculation of the spectral density function involving the N−H groups in proteins. Various equivalent simplifications have since then been proposed that equate the high-frequency components;[19] we refer to these approaches as the reduced spectral density mapping or the high-frequency approximation methods. In the HFA for NH groups, the spectral density function has approximately negligible slope at frequencies > 300 MHz; this approximation becomes almost exact as the molecular weight of the macromolecule increases. Thus, only three rates are needed to evaluate the spectral density function at $J(0)$, $J(\omega_N)$, and $J(\omega_H)$. For carbonyl, if we neglect the dipolar terms in the spectral density functions that depend on frequencies > ω_c, the following equation holds for this HFA:

$$\begin{bmatrix} R_{C'}(C'_{x,y}) \\ R_{C'N}(2N_zC'_z) \\ R_{C'}(C'_z) \end{bmatrix} = \begin{bmatrix} 2(C_1/3 + D_1 + D_2 + 5D_3/4) & 3D_2 & {}^3/_2(D_1 + D_2 + 3D_3 + C_1/3) \\ 0 & 3(D_4 + D_2) + C_2 & 3D_2 + C_1 \\ D_3 & 0 & 3(D_1 + D_2 + D_3) + C_1 \end{bmatrix} \times \begin{bmatrix} J(0) \\ J(\omega_N) \\ J(\omega_C) \end{bmatrix} \quad (8)$$

The constants used above are shown in Table 2.

This approximation is good in practice for mapping the frequencies of motion at 0, ω_N, and $\omega_{C'}$ for large molecules; it may not apply to small molecules, however. The spectral density functions $J(0)$, $J(\omega_N)$, and $J(\omega_{C'})$ are easily expressed in terms of these rates. A linear combination of the rates yields the following simple expressions for the spectral density functions at 0 frequency:

$$J(0) \approx \{2R_{c'}(C'_x) - R_{c'}(C'_z)\}/\{(4\omega_{c'}{}^2\Delta\sigma_g{}^2/9) + 4\sum_j D_{c'j}\} \quad (9)$$

All of the parameters have their previous definitions given in Table 1. Thus, eq 9 allows an estimate of the magnitude of the generalized CSA constant if $J(0)$ is measured independently, for example, from ^{15}N parameters. The hidden assumption is that $J(0)$ from an N−H study is the same as from a C′ study. Alternatively, repeated measurements of $R_{c'}(C'_z)$ and $R_{c'}(C'_x)$

Table 2. Dipolar and CSA Coupling Constants

constant	magnitude (10^9 (rad/s)^2)
$D_1 = D_{CH}{}^{\alpha} + D_{CH}{}^{B} + D_{CH}{}^{N}$ [a]	0.14
$D_2 = D_{CN}$	0.02
$D_3 = D_{CC}{}^{\alpha}$	0.05
$D_4 = D_{NH}{}^{\alpha} + D_{NH}{}^{N}$	1.31
$C_1 = \omega_{C'}{}^2\,\Delta\sigma_g{}^2/3$ [b]	3.85, 6.01, 13.52
$C_2 = C_n = \omega_N{}^2\Delta\sigma_N{}^2)/3$ [c]	0.55, 0.86, 1.9

[a] D_{ij} are the dipolar coupling constants between the two nuclei i and j; the following internuclear distances and gyromagnetic ratios were used: $r_{C'N} = 1.32$ Å, $r_{C'-C}{}^{\alpha} = 1.51$ Å, $r_{C'-H}{}^{N} = 2.64$ Å, $r_{C'-H}{}^{\alpha} = 2.12$ Å, $r_{C'-H}{}^{hb} = 3.0-3.6$ Å, $\gamma_H = 26.7519 \times 10^7$ rad (Ts)$^{-1}$, $\gamma_C = 6.7283 \times 10^7$ rad (Ts)$^{-1}$; $\gamma_N = -2.712 \times 10^7$ rad (Ts)$^{-1}$. [b] $\Delta\sigma_g$ is the generalized CSA coupling constant for the carbonyl carbon. We assume a generalized CSA constant of 170 ppm for the carbonyl carbons (Dayie, K. T.; Wagner, G., unpublished results); the three values are at 9.4, 11.7, and 17.6 T, respectively. [c] We assume a CSA of 160 ppm for the ^{15}N nuclei; the three values are at 9.40, 11.74, and 17.62 T, respectively.

(17) (a) Kay, L. E.; Nicholson, L. K.; Delaglio, F.; Bax, A.; Torchia, D. A. *J. Magn. Reson.* **1992**, *97*, 359−375. (b) Palmer, A. G.; Skelton, N. J.; Chazin, W. J.; Wright, P. E.; Rance, M. *Mol. Phys.* **1992**, *75*, 699−711.

(18) Peng, J. W.; Wagner, G. *Biochemistry* **1992**, *31*, 8571−8586.

(19) (a) Wagner, G. *The 35th Experimental NMR Conference*; Asilomar, California, April 10-15, 1994. (b) Ishima, R.; Nagayama, K. *Biochemistry* **1995**, *34*, 3162−3171. (c) Ishima, R.; Nagayama, K. *J. Magn. Reson. B* **1995**, *108*, 73−76. (d) Peng, J. W.; Wagner, G. *Biochemistry* **1995**, *34*, 16733−16752. (e) Farrow, N. A.; Zhang, O.; Szabo, A.; Torchia, D. A.; Kay, L. E. *J. Biomol. NMR* **1995**, *6*, 153−62.

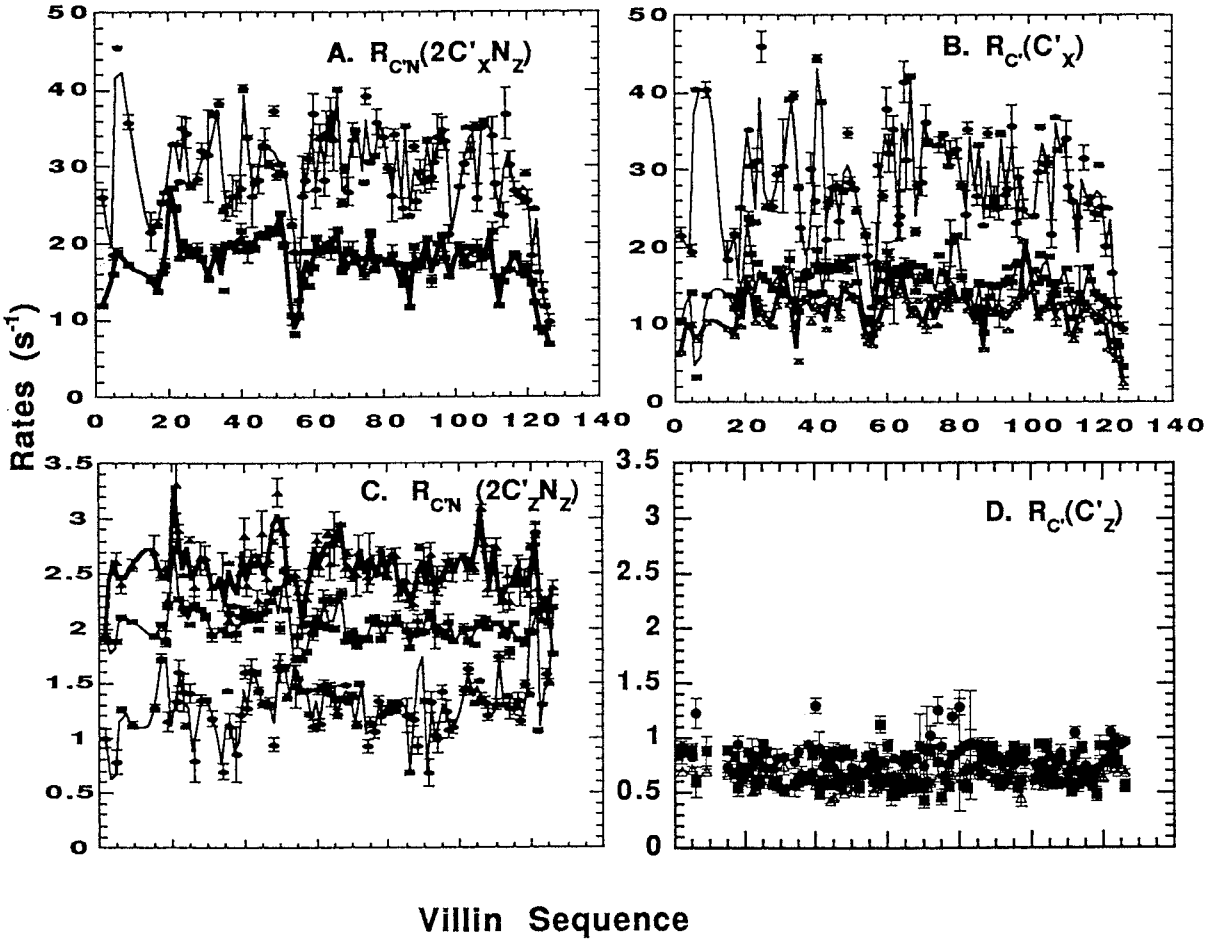

Figure 5. Field dependence of relaxation rates for the protein villin 14T vs amino acid sequence. (**A**) $R_{C'N}(2C'_xN_z)$ at 750 MHz (●) and 500 MHz (■). (**B**) $R_{C'}(C'_x)$ at 750 MHz (●), 500 MHz, (■) and 400 MHz (△). (**C**) $R_{C'N}(2C'_zN_z)$ at 750 MHz (●), 500 MHz (■), and 400 MHz (Δ). (**D**) $R_{C'}(C'_z)$ at 750 MHz (●), 500 MHz (■), and 400 MHz (△).

at different field strengths enables an estimate of the CSA constant. Any three linear combinations of the four rates yield the relevant frequencies shown above, subject to the HFA. The measurement at n different fields provides $2n + 1$ sampling points in the frequency spectrum as well as n independent estimates of $J(0)$. In the next section, we discuss how the values of the spectral density function vary along the backbone with elements of secondary and tertiary structure.

IV. Results

The four relaxation rates $R_{C'}(C'_z)$, $R_{C'N}(2N_zC'_z)$, $R_{C'}(C'_x)$, and $R_{C'N}(2N_zC'_x)$ were measured at three different field strengths. The results are shown in Figure 5. As expected from the relations listed in Table 1, the transverse relaxation rates increase with the field strength. This is due to the dominance of the field dependent CSA contribution and the $J(0)$ contribution which is obviously field independent. The relaxation rate of longitudinal two-spin order, $R_{C'N}(2N_zC'_z)$, shows the opposite behavior, getting smaller with higher field. This is due to the fact that the rate expression lacks a $J(0)$ term and the dipolar and the CSA contributions have opposite field dependence for this size protein. Thus, the field dependence of the $R_{C'N}(2N_zC'_z)$ rates indicates that the dipolar contribution, primarily from the $^1H-^{15}N$ interaction, dominates this rate at lower field strengths. The longitudinal relaxation rate, $R_{C'}(C'_z)$, is essentially field independent apparently because the field dependence of the different contributions counterbalance each other.

V. Discussion

(i) Variation of Spectral Density Functions within the Protein. How is the mobility of the secondary and tertiary structure of the protein villin 14T reflected in the values of the spectral density functions? The values of the spectral density functions at zero frequency [$J(0)$], the nitrogen frequency [$J(\omega_N)$], and the carbonyl frequency [$J(\omega_C)$] allow the quantitation of motions that occur in the millisecond to picosecond range. Regions of the polypeptide chain that are highly constrained have high $J(0)$ and $J(\omega_N)$ values and corresponding small $J(\omega_C)$ values. In contrast, regions displaying unrestricted motions have low values of $J(0)$ and $J(\omega_N)$ and high values of $J(\omega_C)$. Moreover, unusually large values of $J(0)$ are suggestive of exchange contributions to the motion, and unusually small values of $J(0)$ and large values of $J(\omega_C)$ are indicative of very rapid internal motion on the nanosecond to picosecond time scale.

The values of the spectral density function highlight regions along the polypeptide chain of villin 14T that undergo rapid to slow motions on the nanosecond to picosecond time scale. The last four residues (Ser123−Lys126) and the turn connecting β-strands 4 and 5 displayed the most reduced $J(0)$ values and corresponding elevated $J(\omega_{C'})$ values (Figure 6a). These residues show the least restriction to motion: they progressively get floppier and floppier until the last residue Lys126 appears completely unrestricted. Also, relative to the high core $J(0)$ values, the N-terminal helix and the C-terminal β-sheet appear to be more mobile (Figure 6a). These reduced values of $J(0)$ indicate enhanced mobility.

The values of the spectral density function also distinguish clearly between atoms involved in well-defined secondary structural elements such as α-helices and β-sheets, but only weakly differentiate between the different types of secondary

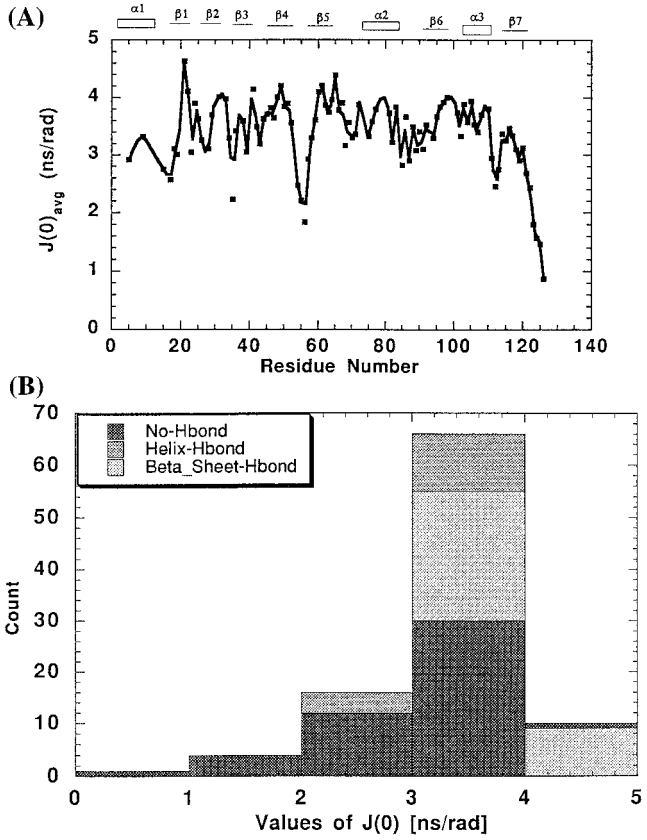

Figure 6. (A) Plots showing variation of the values of the spectral density function at 0 frequency with the villin 14T amino acid sequence. The average of $J(0)$ at 9.4, 11.74, and 17.62 T is plotted. Note the rather large variation in mobility exhibited by $J(0)$ with the protein sequence and secondary structural elements indicated at the top of the figure. Errors estimates are about 5−15% based on repeated measurements of the rates. (B) A histogram of the distribution of $J(0)$ values with the hydrogen-bonded state of atoms found in α-helices (residues 1−11, 71−88, and 104−110), β-sheets (residues 17−24, 27−31, 37−41, 43−53, 56−66, 92−98, and 114−118), and carbonyl groups not involved in intramolecular hydrogen-bonds (remainder of the analyzed residues). The selection was made by inspecting the solution structure of villin 14T.[7b] The average values for the β-sheet, α-helix, and other residues are 3.77, 3.20, and 3.06 ns/rad, respectively.

structure (Figure 6A). Elements of well-defined structure such as α-helices and β-strands have high $J(0)$ values. On average, the values for residues found in β-sheets are higher than those found in α-helices[4b] (Figure 6A). Notably, most of the residues that show the highest values are involved in hydrogen-bonding as determined by the solution structure, but not all hydrogen-bonded residues have high values (Figure 6B). Because it is not clear yet how general this observation is, it remains to be seen if it will hold for other proteins as well.

Nonetheless, these effects are mirrored, with decreasing resolution, in the other values of the spectral density functions (Figure 7). For example, $J(40)$ shows the gross features of what is clear at $J(0)$, but $J(50)$ does less so. Regions of rapid internal motion are reflected in reduced values of $J(0)$ ↔ $J(50)$, but increased $J(100)$ ↔ $J(188)$. Inordinately large $J(0)$ with corresponding average $J(40)$, $J(50)$, and $J(75)$ values are suggestive of slow motions on the microsecond time scale. Because errors range from 5 to 15%, only differences greater than 15% might be significant. The values obtained at 750 MHz have larger errors because of the overall weak signal-to-noise at this frequency. The higher frequency components display behavior complementary to those observed at lower frequency. Picosecond motions are better reflected in the values of the

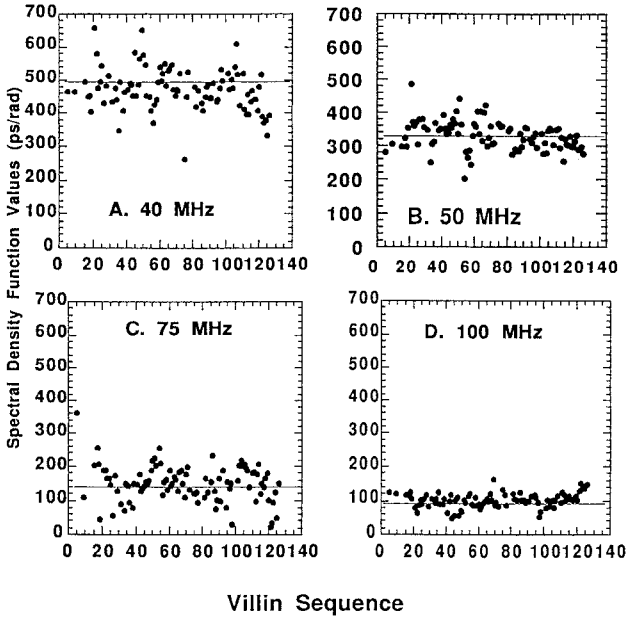

Figure 7. Variation of the values of the spectral density function vs amino acid sequence in villin 14T. The values at ω_N are given as measured at three field strengths: (**A**) 9.4 T, (**B**) 11.7 T, and (**C**) 17.6 T. **D** shows the spectral density function at $\omega_{C'}$ determined at 17.6 T.

spectral density function at the carbonyl frequency. Regions of least restriction have high values at the carbonyl frequencies, whereas regions of high restriction exhibit low values.

Figure 8 shows the frequency map for several representative residues along the protein backbone. On average the values of the spectral density function of β-sheet residues (Figure 8A) are slightly higher than those in α-helices (Figure 8C), and those at the ends of the protein (Figure 8D) have substantially lower values than loops (Figure 8B). Interpreting these differences as due to purely geometric variations rests on the assumption that the CSA constant is roughly the same for all residues. This might be invalid. Indeed there is no consensus on the magnitude of carbonyl CSA anisotropy; preliminary results indicate the CSA may vary by as much as 130−180 ppm along the backbone (Dayie, K. T.; Wagner, G., unpublished results). The variations in the relaxation rates are therefore a complex interplay of both the CSA "constants" and the spectral densities. This is a major limitation of the quantitative use of the carbonyl as a probe of dynamics along the backbone. Nonetheless, the large differences between loops, terminal ends, and well-structured parts of the protein can be qualitatively ascribed to changes in geometric quantities such as spectral densities.

A compensatory behavior is also revealed by the anticorrelation of $J(0)$ and $J(\omega_C)$ (Figure 9). Depending on the spectrometer frequency and the size of the protein, $J(\omega_N)$ and $J(0)$ are correlated (small proteins, low spectrometer field) or anticorrelated (large proteins, high spectrometer field). The same holds true for correlations between $J(\omega_C)$ and $J(0)$. Note also that the spread is much larger at higher frequencies probably because of larger errors associated with these values.

(ii) Determining Overall Tumbling: R_2/R_1 Ratio vs Linear Correlation of $J(\omega_x)$ with $J(0)$. In the analysis of heteronuclear ^{15}N relaxation parameters including T_1, T_2, and heteronuclear NOE, Kay, Torchia, and Bax suggested using the R_2/R_1 ratios that fall within one standard deviation of the mean for determining the overall tumbling of isotropically reorienting spheroids.[20] This is valid for residues with internal motions

(20) Kay, L. E.; Torchia, D. A.; Bax, A. *Biochemistry* **1989**, *28*, 8972−8979.

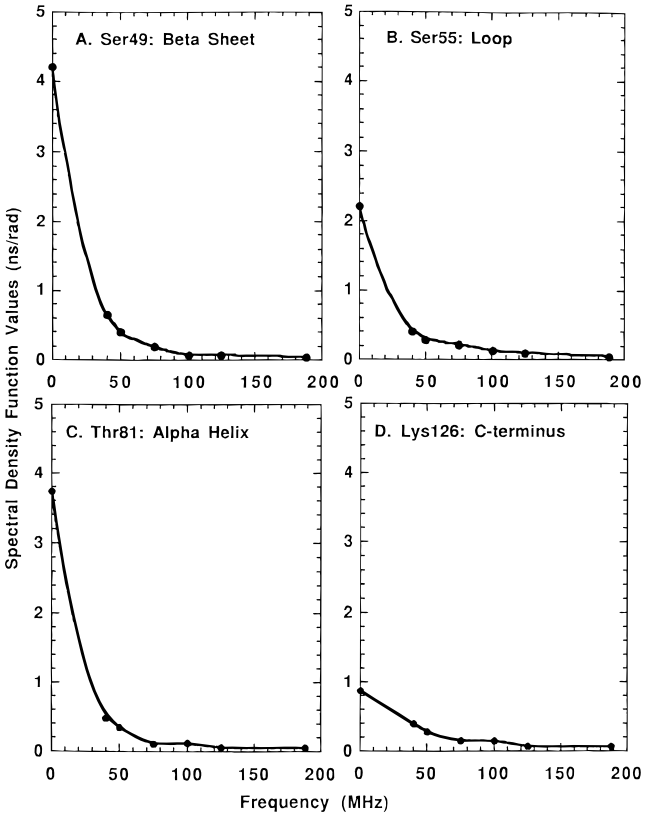

Figure 8. Frequency spectrum of four residues in different regions of the polypeptide chain: (**A**) Ser 49, a residue in an antiparallel β-sheet; (**B**) Ser 55, a residue in a long loop; (**C**) Thr 81, a residue in an α-helix; **(D**) Lys 126, a residue in C-terminus. Errors range from 5 to 15%. The values obtained at 750 MHz have larger errors because of the overall weak signal-to-noise at this frequency.

satisfying the extreme narrowing condition ($\omega\tau_i \ll 1$) and order parameters typical for secondary structural elements ($S^2 > 0.6$). It has recently been shown that the $J(0)$ and $J(\omega_N)$ are linearly correlated for nearly all proteins for which such studies were carried out,[3b,21] thus:

$$J(\omega_N) = \alpha J(0) + \beta \qquad (10)$$

α and β are the slope and intercept of the linear fit. A Lorentzian spectral density function $J(\omega) = 2\tau/5(1 + \omega^2\tau^2)$ leads to a third degree equation in τ:

$$\tau^3(2\alpha\omega_N^2) + \tau^2(5\beta\omega_N^2) + \tau\{2(\alpha - 1)\} + 5\beta = 0 \qquad (11)$$

The positive roots (τ) of this equation give the correlation times of the various motions contributing to the low-frequency part of the spectral density function. This approach applied to the carbonyl data yields values comparable to the ^{15}N case. As in the former case, the first root has no physical meaning. The second and third roots, on the basis of their magnitudes, are assigned, respectively, to the overall tumbling of the molecule and a generalized internal motion time constant. In the current analysis we obtain an overall tumbling time constant of 10.3 ns which compares quite well with previous determinations using ^{15}N-only data that gave 10.2 ns (using eq 11 above) and 10.5 ± 0.2 ns using Lipari−Szabo formalism.[7a] This methodology is inapplicable in cases where the molecule tumbles anisotropically.

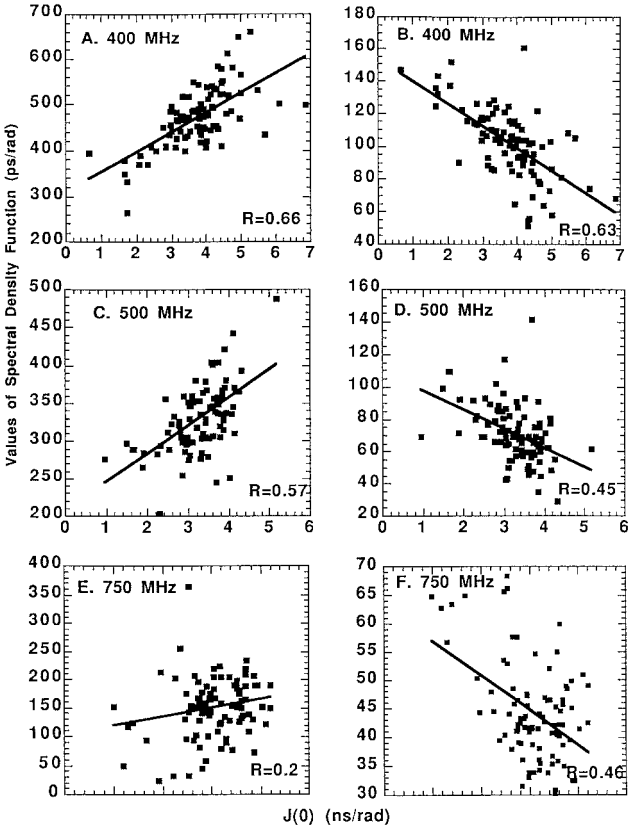

Figure 9. Plots of $J(\omega_N)$ (**A, C, E**) and $J(\omega_{C'})$ (**B, D, F**) as a function of $J(0)$ at three field strengths. The correlation coefficients are given in the lower right-hand corners of each plot.

(iii) Comparison of Dynamics of ^{13}C Carbonyl and ^{15}N Spins. Given the success of ^{15}N backbone studies, why do we need another probe of mobility? In addition to the reason enumerated in the introduction, the first comparative analysis done on the dynamics of backbone nitrogen and the carbonyl spins indicated similarities and significant differences.[4] Here, we expand on those initial studies. Both the carbonyl ^{13}C and the amide ^{15}N form part of the same planar peptide unit. One may, therefore, expect both nuclei to exhibit similar relaxation behavior. To the extent that both ^{13}C′ and ^{15}N transverse rates correlate with the regular secondary structural elements and the nonregular elements,[4] this is probably true. Loops and untethered terminal residues always display reduced rates for both nuclei, and helices and β-sheets have uniformly elevated rates. Regions of restricted or small amplitude motions, as is usually found in such well-defined structural elements, exhibit high $J(0)$ values, whereas regions of enhanced mobility or large amplitude fluctuations commonly found in loops and regions of low persistence structure have reduced $J(0)$ values. Figure 10 displays a comparative plot of both $J(0)$ and $J(\omega_N)$ determined by ^{15}N-only and ^{13}C-carbonyl-only measurements. The correlation between the two is quite high suggesting both measurements provide the same level of information. Like the nitrogen atom, the carbonyl ^{13}C carbon spin is a useful selective-pass filter of the frequencies (at 0, ω_N and $\omega_{C'}$) of motion along the protein backbone. In this regard, the carbonyl nuclei like the ^{15}N nuclei are comparable probes of the dynamic heterogeneity along the protein backbone.

Beyond the obvious similarities described above, a number of significant differences exist, however. Unlike that of the nitrogen atom, the CSA of the carbonyl carbon atoms dominates

(21) (a) Lefèvre, J.-F.; Dayie, K. T.; Peng, J. W.; Wagner, G. *Biochemistry* **1996**, *35*, 2674−2686. (b) Dayie, K. T.; Lefèvre, J.-F.; Wagner, G. In *Dynamics and the problem of molecular recognition in Biological Macromolecules*; NATO ASI Series A288; Jardetsky, O., Lefèvre, J.-F., Eds.; Plenum: New York, 1996; pp 139−162.

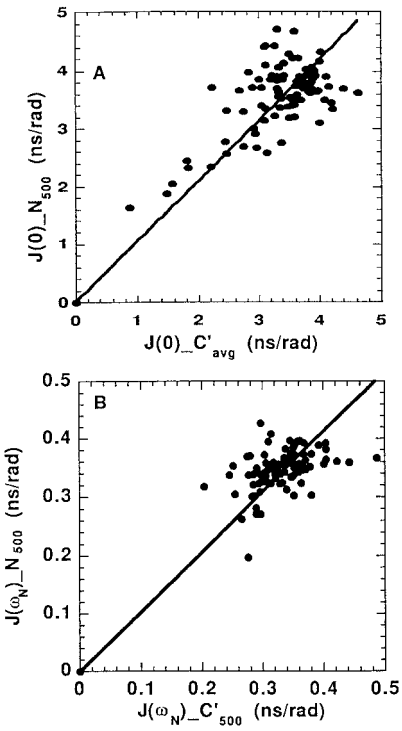

Figure 10. (**A**) Comparison of $J(0)$ as obtained by ^{15}N-only and ^{13}C-carbonyl-only measurements. (**B**) Comparison of $J(\omega_N)$ as obtained by ^{15}N-only and ^{13}C-carbonyl-only measurements.

the relaxation. This dominance has some clear implications. First, the carbonyl carbon may be more sensitive to the hydrogen-bonding state than the ^{15}N nuclei. This is confirmed only approximately by our current data. For instance, residues involved in hydrogen-bonding as determined by the solution structure[7b] usually have large rates and $J(0)$ values; however, not all residues with large rates and $J(0)$ values are hydrogen-bonded (Figure 6B). Second, whereas the ^{15}N data do not distinguish between elements of secondary structure, the current data points to the possibility that β-sheets might have larger $J(0)$ values than helices (Figure 6B, Figure 8). This is consistent with the notion that hydrogen-bonds in β-sheets are shorter in the average than those in helices.[22] However, the precision of the current measurements does not allow such a clear cut distinction to be made. Third, the carbonyl tensor is expected to point in a direction different from the N−H vector and the ^{15}N tensor. Thus, studies of the carbonyl carbon could open up new avenues for probing motional anisotropy along the backbone. Furthermore, because Gln and Asn side chains are usually found in active sites, an extension of the current proposed experiments could potentially allow direct measures of the effect of ligand binding. Finally, it has not escaped our attention that HCN-type experiments currently used in RNA assignments are identical to HNCO experiment.[23] Therefore the methodology outlined in this paper can be fruitfully modified for the studies of RNA dynamics. These are currently under investigation.

Acknowledgment. We are grateful to Professor Jean-François Lefèvre and Dr. Jeffrey W. Peng for many useful discussions. We are indebted to Dr. Igor Najfeld for many stimulating discussions on use of matrix exponentials. We thank Dr. Larry Werbelow for very useful and critical comments on interference effects. We thank Dr. Michelle Markus and Professor Paul Matsuidaira for the villin sample used in this work. This work was supported by NIH grant GM47467 and NSF grant MCB9316938.

Supporting Information Available: Four tables with the measured rate constants (8 pages). See any current masthead page for ordering and Internet access instructions.

JA9633880

(22) Jeffrey, G. A.; Saenger, W. *Hydrogen Bonding in Biological Structures;* Springer-Verlag: New York, 1991.

(23) (a) Sklenar, V.; Peterson, R. D.; Rejante, M. R.; Wang, E.; Feigon, J. *J. Am. Chem. Soc.* **1993**, *115*, 12181−12182. (b) Farmer, B. T., II; Mueller, L.; Nikonowicz, E. P.; Pardi, A. J. *J. Am. Chem. Soc.* **1993**, *115*, 11040−11042. (c) Tate, S-i.; Ono, A.; Kainosho, M. *J. Am. Chem. Soc.* **1994**, *116*, 5977−5978.

(24) Shaka, A. J.; Keeler, J.; Frenkiel, T.; Freeman, R. *J. Magn. Reson.* **1983**, *52*, 335−338.

(25) (a) McCoy, M.; Mueller, L. *J. Am. Chem. Soc.* **1992**, *114*, 2108−2112. (b) McCoy, M.; Mueller, L. *J. Magn. Reson.* **1992**, *98*, 674−679.

(26) (a) Kupce, E.; Boyd, J.; Campbell, I. D. *J. Magn. Reson. B* **1995**, *106*, 300−303. (b) Kupce, E.; Freeman, R. *J. Magn. Reson. A* **1993**, *105*, 234−238.

(27) Sklenar, V.; Piotto, M.; Leppik, R.; Saudek, V. *J. Magn. Reson. A* **1993**, *102*, 241−245.

(28) Cavanagh, J.; Palmer, A. G., III; Wright, P. E.; Rance, M. *J. Magn. Reson.* **1991**, *91*, 429−436.

(29) (a) Koetzle, T. F.; Hamilton, W. C.; Parthasarathy, R. *Acta Crystallogr*. **1972**, *B28*, 2088−2090. (b) Faucett, J. K.; Camerman, N.; Carman, A. *Acta Crystallogr*. **1975**, *B31*, 658−665. (c) Harris, R. K. *Nuclear Magnetic Resonance Spectroscopy: A Physico-Chemical View*; Longman Group: Essex, U.K., 1983; pp 1−260. (d) Hiyama, Y.; Niu, C.; Silverton, J. V.; Bavoso, A.; Torchia, D. A. *J. Am. Chem. Soc.* **1988**, *110*, 2378−2383.